Occupancy Grid Mapping for Automotive Driving Exploiting Clustered Sparsity

Önen, Çağan ; Pandharipande, Ashish ; Joseph, Geethu; Myers, Nitin Jonathan

DOI
10.1109/JSEN.2023.3342463

Publication date
2024

Document Version
Final published version

Published in
IEEE Sensors Journal

Citation (APA)
Önen, Ç., Pandharipande, A., Joseph, G., & Myers, N. J. (2024). Occupancy Grid Mapping for Automotive Driving Exploiting Clustered Sparsity. *IEEE Sensors Journal*, *24*(7), 9240-9250.
https://doi.org/10.1109/JSEN.2023.3342463

Occupancy Grid Mapping for Automotive Driving Exploiting Clustered Sparsity

Çağan Önen, Ashish Pandharipande, *Senior Member, IEEE*, Geethu Joseph, *Member, IEEE*,
and Nitin Jonathan Myers, *Member, IEEE*

***Abstract*—Occupancy grid maps provide information about obstacles and available free space in the environment and are crucial in automotive driving applications. An occupancy map is constructed using point cloud data from sensor modalities such as light detection and ranging (LiDAR) and radar used for automotive perception. In this article, we formulate the problem of estimating the occupancy grid map using sensor point cloud data as a sparse binary occupancy value reconstruction problem. Our proposed occupancy grid estimation method, based on pattern-coupled sparse Bayesian learning (PC-SBL), leverages the sparsity and spatial dependencies inherent in occupancy maps typically encountered in automotive scenarios. The proposed method shows enhanced detection capabilities compared to two benchmark methods based on performance evaluation with scenes from the nuScenes and RADIal public datasets.**

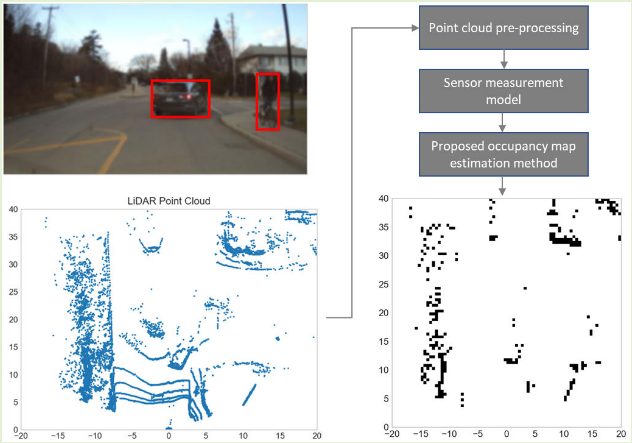

***Index Terms*— Light detection and ranging (LiDAR), nuScenes dataset, occupancy grids, pattern-coupled prior, radar, RADIal dataset, sensor point clouds, spatial correlation.**

I. INTRODUCTION

THE development of advanced driver assistance systems and autonomous driving technologies is gaining significant momentum, given its potential to increase safety and convenience in driving on the road. A holistic solution for ensuring safe driving with increased autonomy involves two key components: 1) an environment perception engine that uses real-time sensor data and 2) a proactive decision-making engine leveraging perceived information and object dynamics to make real-time decisions. The focus of this work is on the former: to develop an algorithm to obtain an accurate perception and understanding of the surrounding environment [1], [2]. Occupancy map estimation plays a vital role in this process, providing a grid map representation of the occupancy status of the surrounding space using sensor data [3], [4]. It provides information about the presence or absence of obstacles in each grid within a given space. This work considers the occupancy map estimation problem using point cloud data derived from sensors such as light detection and ranging (LiDAR) and radar, commonly used to support advanced driver assistance systems and autonomous driving applications.

Occupancy map building has been studied extensively in robotics [3], [5], [6], [7] and for autonomous driving applications [8], [9], [10]. The popular occupancy map estimation methods use the inverse-sensor model [5], [11] and kernel-based approaches [12], [13]. The inverse-sensor model approach is computationally simple. However, it suffers from occupancy estimation conflicts when combining multiple measurements with partially overlapping fields of view. It also overlooks the spatial correlation within the map, leading to less accurate occupancy map estimates and sensitivity to sensor noise. This problem is handled using a Gaussian process to model the spatial dependencies at the expense of increased computational complexity [12]. An improved version of this approach, Bayesian generalized kernel (BGK)-based mapping [13], addressed the complexity issue. However, the above mapping algorithms [5], [11], [12], [13] developed for robotic applications do not exploit contextual information and the underlying sparse structure in occupancy maps for automotive

Manuscript received 16 August 2023; revised 30 November 2023; accepted 1 December 2023. Date of publication 19 February 2024; date of current version 2 April 2024. The associate editor coordinating the review of this article and approving it for publication was Prof. Domenico Ciuonzo. *(Corresponding author: Ashish Pandharipande.)*

Çağan Önen was with NXP Semiconductors, 5656 AG Eindhoven, The Netherlands, and also with the Delft University of Technology, 2628 CD Delft, The Netherlands.

Ashish Pandharipande is with NXP Semiconductors, 5656 AG Eindhoven, The Netherlands (e-mail: ashish.pandharipande@nxp.com).

Geethu Joseph is with the Faculty of Electrical Engineering, Mathematics, and Computer Science, Delft University of Technology, 2628 CD Delft, The Netherlands (e-mail: g.joseph@tudelft.nl).

Nitin Jonathan Myers is with the Faculty of Mechanical Engineering, Delft University of Technology, 2628 CD Delft, The Netherlands (e-mail: n.j.myers@tudelft.nl).

Digital Object Identifier 10.1109/JSEN.2023.3342463

driving. Such contextual information can be street topology, which can be derived from navigation maps. The sparse structure arises because, even in the presence of obstacles, only the borders or edges of objects are reflected in the map. To this end, we present an occupancy map estimation method that exploits both sparsity and spatial correlation within the occupancy map.

Our approach relies on a signal model using preprocessed sensor point cloud measurements. The preprocessing uses digital map information to define focus areas of interest in an automotive driving application. Digital map information has also been used in other works, such as [4] and [14], to characterize drivable spaces from nondrivable spaces. Having defined the focus area, we construct a linear occupancy map measurement for each point within the point cloud, corresponding to the LiDAR or radar. Then, we leverage the pattern-coupled sparse Bayesian learning (PC-SBL) framework [15] for occupancy grid map estimation from the linear measurements. In the PC-SBL framework, the sparse structure is captured via a sparsity-promoting prior distribution on the map, and the spatial dependencies are exploited by assuming a block-sparse structure for the map. This assumption is valid since real-world obstacles span multiple occupancy grid cells for typical LiDAR and radar resolutions. PC-SBL estimates block-sparse vectors without assuming the block size, making it promising for automotive driving applications where prior knowledge of the object sizes is unavailable.

We evaluate our method using LiDAR and radar point cloud data from the nuScenes and RADIal datasets [16], [17], [18]. For the benchmarks, we use the occupancy map estimation methods in [5] and [13]. We use an angular scan normalized mean-squared error (NMSE) and intersection over bounding box (IoBB) metric for quantitative comparison of the methods. The evaluation shows that the proposed approach outperforms the benchmark methods by resolving obstacles better and eliminating road reflections in some scenes.

We extend our earlier work [19] in multiple directions. First, while we focus on LiDAR point cloud data in [19], we generalize our sensor signal model presented in Section II to encompass radar point cloud data. Second, in Section III, we expand the description of the PC-SBL occupancy map estimation algorithm. Finally, in Section IV, we expand the performance evaluation results to include radar data from the nuScenes and RADIal public datasets. In particular, we note that the radar data in nuScenes and RADIal have different resolutions. This allows us to evaluate the impact of different point cloud resolutions on the occupancy mapping method.

II. OCCUPANCY MAP MEASUREMENT MODEL

The occupancy map of an environment is defined over a grid, where each cell represents a discrete location in 2-D. The map consists of probability values that indicate the likelihood of each cell being occupied. Typically, these probabilities are updated using point cloud data acquired by the ego vehicle through LiDAR or radar sensors [1], [20]. In this section, we discuss constructing a linear occupancy map measurement model using the acquired point cloud information.

A. Data Preprocessing

To preprocess and prepare the input to our estimation algorithm, we first exclude point cloud data corresponding to the cells that fall outside the range and elevation of interest. Subsequently, we obtain a collection of points in the 2-D plane from the 3-D points by discarding z-coordinate information. Let M denote the remaining number of sensor measurement points, referred to as reflection points, representing potential occupancy locations inside the region of interest. The points from which no reflections are observed are called free-space points. Each of the M sensor measurements consists of the 3-D coordinates of a reflection point, denoted by $\mathbf{x}_m$, which are represented in the global coordinate system using the ego vehicle's position as the origin.

We further process the measurements to reduce the dimension of the occupancy map to be estimated. To this end, we include contextual information from digital maps [21] in the model by defining a *focus area*. It comprises the cells of interest, i.e., the cells on the ego vehicle's road and the walkways around [14]. The area beyond the walkways is ignored as it is not crucial for driving scenarios. In practice, the borders of the focus area can be obtained from digital mapping services [21]. The focus area is then partitioned into N 2-D cells. Then, the reflection points and free-space points are discretized to the nearest grid cells. These points are then represented using the indices of the corresponding grid cells. We use $\mathbf{f} \in \mathbb{R}^N$ to denote the unknown map vector comprising the occupancy probabilities of the N cells, representing the occupancy grid map. The goal is to estimate this map vector $\mathbf{f}$ from the M point cloud measurements.

B. LiDAR-Based Occupancy Map Measurement Model

We now construct a linear measurement model of the map vector $\mathbf{f}$ using the M LiDAR point cloud measurements. Each LiDAR point cloud measurement indicates that the corresponding reflection point (discretized to the nearest grid cell) is occupied, and the cells along the line connecting the ego vehicle and reflection point are unoccupied. If the cell corresponding to the nth entry of $\mathbf{f}$ is a reflection point, we set $f_n = y_{\text{occ}}$. Here, y_{occ} is a parameter close to 1 to indicate that the cell is likely to be occupied. In compact form

$$\mathbf{e}_n^{\mathsf{T}}\mathbf{f} = y_{\text{occ}} \tag{1}$$

when a reflection is observed from a cell indexed n, where $\mathbf{e}_n \in \{0, 1\}^N$ denotes the nth column of the identity matrix.

We define $\mathcal{F}_n$ as a set that contains indices of the cells sampled along the line from the ego vehicle to the nth cell. The probability that all these cells are unoccupied is $\prod_{k\in\mathcal{F}_n}(1 - f_k)$. For every index $k \in \mathcal{F}_n$, f_k is expected to be small as the corresponding cell is likely to be unoccupied. Under this assumption, $\prod_{k\in\mathcal{F}_n}(1 - f_k) \approx 1 - \sum_{k\in\mathcal{F}_n} f_k = 1 - \sum_{k\in\mathcal{F}_n} \mathbf{e}_k^{\mathsf{T}}\mathbf{f}$. We set this approximation equal to $1 - y_{\text{free}}$, where y_{free} is a parameter chosen to be close to 0. Therefore,

$$\sum_{k\in\mathcal{F}_n} \mathbf{e}_k^{\mathsf{T}}\mathbf{f} = y_{\text{free}}. \tag{2}$$

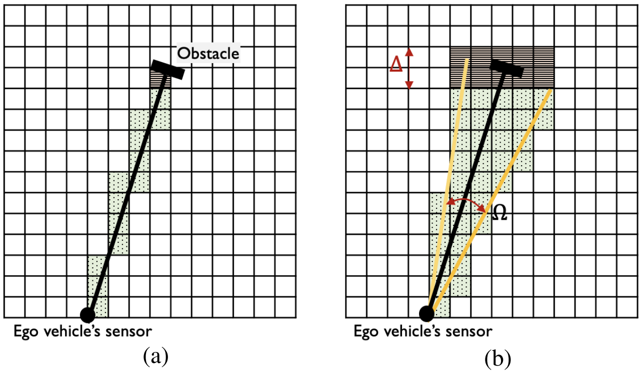

Fig. 1. For LiDAR point clouds, our method labels all the cells along the line between the sensor and a reflection point as free. For sparse radar point clouds, the cells within a beamwidth of Ω are labeled as free, and those in a region of width Δ around the reflection point are labeled as occupied. (a) LiDAR sensor model. (b) Radar sensor model.

In short, each LiDAR point cloud reflection results in two linear measurements of the occupancy map as given in (1) and (2). A collection of M point cloud reflections thus leads to $2M$ linear equations of $\mathbf{f}$ given by

$$\mathbf{y} = \mathbf{C}\mathbf{f} + \mathbf{w}. \tag{3}$$

Here, $\mathbf{w} \in \mathbb{R}^{2M}$ is modeled as independent and identically distributed Gaussian measurement noise with zero mean and unknown variance σ^2. Also, $\mathbf{C} \in \{0, 1\}^{2M\times N}$ is a selection matrix defined by (1) and (2). Specifically, if the mth reflection point corresponds to the nth entry of $\mathbf{f}$, we set $y[2m-1] = y_{\text{occ}}$ and $y[2m] = y_{\text{free}}$. Also, the $(2m-1)$th and $2m$th rows of $\mathbf{C}$ are $\mathbf{e}_n^{\mathsf{T}}$ and $\sum_{k\in\mathcal{F}_n} \mathbf{e}_k^{\mathsf{T}}$, respectively.

C. Radar-Based Occupancy Map Measurement Model

In this section, we construct a linear measurement model of the map vector $\mathbf{f}$ using the M radar point cloud measurements. We observed that the point cloud density in the radar dataset used in this article is significantly lower than that in the LiDAR dataset. Using such low-density points results in poor occupancy grid map estimates than the LiDAR-based approach. To address this issue, we adopt the approach proposed in [11] wherein a conical beam originating at the ego vehicle's sensor is constructed for each point cloud measurement. This beam has a width of Ω and terminates in a region of width Δ about the reflection point, as shown in Fig. 1(b). The region where the beam terminates is marked using dashed cells, while the remaining cells within the conical beam are represented as dotted cells. We use $\mathcal{O}_n$ and $\mathcal{F}_n$ to denote the sets comprising the indices of the dashed cells and dotted cells, respectively. Similar to our LiDAR-based measurement model, we define two measurements of the occupancy map using these sets

$$\sum_{k\in\mathcal{F}_n} \mathbf{e}_k^{\mathsf{T}}\mathbf{f} = y_{\text{free}}, \quad \text{and} \quad \sum_{k\in\mathcal{O}_n} \mathbf{e}_k^{\mathsf{T}}\mathbf{f} = y_{\text{occ}}. \tag{4}$$

While our LiDAR-based model labels a single cell as occupied for a reflection point, our radar-based model marks all the cells within $\mathcal{O}_n$ as occupied for the same point. Here, the motivation is to fill the gaps between the sparse radar point data and represent the region's obstacles using several cells. A linear measurement model similar to (3) can be constructed, by putting together (4) for all the M measurements. In the radar case, if the mth reflection point corresponds to the nth entry of $\mathbf{f}$, we set the $(2m-1)$th and $2m$th rows of $\mathbf{C}$ as $\sum_{k\in\mathcal{O}_n} \mathbf{e}_k^{\mathsf{T}}$ and $\sum_{k\in\mathcal{F}_n} \mathbf{e}_k^{\mathsf{T}}$, respectively.

III. OCCUPANCY MAP ESTIMATION USING PC-SBL

The occupancy map estimation problem is to find the map vector $\mathbf{f}$ from linear measurements of the form $\mathbf{y} = \mathbf{C}\mathbf{f} + \mathbf{w}$. In this section, we develop a PC-SBL-based method that uses information from these linear measurements and exploits the block-sparse structure in map vector $\mathbf{f}$ for maximum a posteriori probability (MAP)-based inference.

In the PC-SBL framework, the vector to be estimated, i.e., $\mathbf{f}$, is modeled as a realization of a random variable. The distribution on $\mathbf{f}$ is modeled as a Gaussian hierarchical prior. Specifically,

$$p(\mathbf{f}|\boldsymbol{\alpha}) = \prod_{n=1}^{N} p(f[n]|\boldsymbol{\alpha}) = \prod_{n=1}^{N} \mathcal{N}\Big(0, \big(\alpha[n] + \beta \sum_{j\in\mathcal{L}_n} \alpha[j]\big)^{-1}\Big). \tag{5}$$

Here, $\boldsymbol{\alpha} \in \mathbb{R}^N$ is an unknown hyperparameter vector that controls the sparsity of $\mathbf{f}$, the prefixed coupling parameter $\beta \in [0, 1]$ models the spatial correlation within $\mathbf{f}$, and $\mathcal{L}_n$ denotes the set of immediate neighbors (the adjacent left, right, above, and below cells) of the nth cell. We observe that the Gaussian prior in (5) becomes increasingly concentrated at zero for a large α_n. This behavior promotes sparsity, encouraging f_n to be close to zero when α_n is high. We also observe that the prior corresponding to the cell indexed n concentrates at zero if any of the neighboring hyperparameters in $\boldsymbol{\alpha}_{\mathcal{L}_n}$ increases. The coupled structure in (5) thus enforces block sparsity in $\mathbf{f}$.

We use a Gamma prior on the hyperparameter $\boldsymbol{\alpha}$ and the inverse of the noise variance $\gamma = \sigma^{-2}$, as discussed in the SBL hierarchical model [22]. These Gamma priors are parameterized by $a, b, c, d > 0$ as shown in the following:

$$p(\boldsymbol{\alpha}) = \prod_{n=1}^{N} \Gamma\left(\alpha[n] \mid a, b\right) = \prod_{n=1}^{N} \Gamma(a)^{-1} b^a \alpha[n]^a e^{-b\alpha[n]} \tag{6}$$

$$p(\gamma) = \Gamma(\gamma \mid c, d) = \Gamma(c)^{-1} d^c \gamma^c e^{-d\gamma}. \tag{7}$$

Due to the linear model in (3) and the use of Gaussian priors for the occupancy map and noise, it can be shown that the posterior $p(\mathbf{f}|\mathbf{y}, \boldsymbol{\alpha}, \gamma)$ is Gaussian.

With the above hierarchical prior model, we use type II MAP estimation of $\mathbf{f}$ where we first estimate the parameters $\boldsymbol{\alpha}$ and γ from the measurement vector $\mathbf{y}$. The estimated hyperparameters, $\hat{\boldsymbol{\alpha}}$ and $\hat{\gamma}$, are then used to compute the MAP estimate of $\mathbf{f}$, which is the mean of the Gaussian distribution $p(\mathbf{f}|\mathbf{y}, \hat{\boldsymbol{\alpha}}, \hat{\gamma})$. The hyperparameter estimation relies on the iterative expectation–maximization (EM) method, with $\mathbf{f}$ being the unobserved latent variable. The tth iteration of the resulting EM algorithm is given by

$$\alpha_t[n] = \frac{a}{0.5\hat{\nu}_t[n] + \beta \sum_{j\in\mathcal{L}_n} \hat{\nu}_t[j] + b}, \tag{8}$$

Algorithm 1 Occupancy Map Estimation Using PC-SBL

```
Input: Reflection point coordinates $\{\mathbf{x}_m\}_{m=1}^{M}$
Parameters: Coupling parameters $\beta$, Gamma distribution parameters $a, b, c, d > 0$
Output: Binary occupancy grid map: $\hat{\mathbf{g}}$
For each measurement $m$ do
    if (sensor == LiDAR) then
        $n \leftarrow$ index of the reflection point $\mathbf{x}_m$ in $\mathbf{f}$
        $\mathcal{F}_n \leftarrow$ indices of (sampled) cells between vehicle and $\mathbf{x}_m$
        $(2m-1)$th row of $\mathbf{C} \leftarrow \mathbf{e}_n^{\mathsf{T}}$
    if (sensor == Radar) then
        $\mathcal{O}_n \leftarrow$ indices inside the radar conical beam for $\mathbf{x}_m$
        $\mathcal{F}_n \leftarrow$ indices of the conical beam's terminal points
        $(2m-1)$th row of $\mathbf{C} \leftarrow \sum_{k\in\mathcal{O}_n} \mathbf{e}_k^{\mathsf{T}}$
    $2m$th row of $\mathbf{C} \leftarrow \sum_{k\in\mathcal{F}_n} \mathbf{e}_k^{\mathsf{T}}$
    $y[2m-1] \leftarrow y_{\text{occ}}$
    $y[2m] \leftarrow y_{\text{free}}$
Initialize $t = 0$, $\alpha_t = \mathbf{1}$ and $\gamma_t = 1$
repeat
        Compute $\mathbf{D}_t$ using (10) and $\nu_t$ from (11)
        Update $\alpha_t$, $\gamma_t$ using (8), (9)
        $t \leftarrow t+1$
until convergence
Compute $\hat{\mathbf{g}}$ from (15)
```

$$\gamma_t = \frac{\|\mathbf{y} - \mathbf{C}\hat{\boldsymbol{\mu}}_t\|_2^2 + \gamma_{t-1}^{-1}\sum_n \hat{\Phi}_t[n,n]D_t[n,n] + 2d}{M+2c} \tag{9}$$

where we define $\mathbf{D}_t$ as a diagonal matrix with

$$D_t[n,n] = \alpha_{t-1}[n] + \beta \sum_{j\in\mathcal{L}_n} \alpha_{t-1}[j] \tag{10}$$

and $\hat{\nu}_t \in \mathbb{R}^N$ is the vector of second moments of entries of $\mathbf{f}$ given $\gamma_{t-1}, \boldsymbol{\alpha}_{t-1}$, and $\mathbf{y}$

$$\hat{\nu}_t[n] = \hat{\mu}_t[n]^2 + \hat{\Phi}_t[n,n] \tag{11}$$

$$\hat{\boldsymbol{\mu}}_t = \gamma_{t-1}\hat{\boldsymbol{\Phi}}_t\mathbf{C}^T\mathbf{y} \tag{12}$$

$$\hat{\boldsymbol{\Phi}}_t = (\gamma_{t-1}\mathbf{C}^T\mathbf{C} + \mathbf{D}_t)^{-1}. \tag{13}$$

We refer the interested reader to [15] for a comprehensive derivation of the EM algorithm. The EM updates above are iteratively performed until convergence. After convergence, the vector $\hat{\boldsymbol{\mu}}_t$ is the MAP estimate of the unknown occupancy map that is $\hat{\mathbf{f}} = \hat{\boldsymbol{\mu}}_t$, which is the mean of the converged Gaussian distribution $p(\mathbf{f}|\mathbf{y}, \boldsymbol{\alpha}_t, \gamma_t)$. A summary of the proposed PC-SBL-based algorithm is given in Algorithm 1.

The computational complexity of the PC-SBL algorithm is primarily determined by the E-step in (13). Therefore, using the matrix inversion lemma, we can rewrite (13) as

$$\hat{\boldsymbol{\Phi}}_t = \mathbf{D}_t^{-1} - \mathbf{D}_t^{-1}\mathbf{C}^T(\gamma_{t-1}^{-1}\mathbf{I} + \mathbf{C}\mathbf{D}_t^{-1}\mathbf{C}^T)^{-1}\mathbf{C}\mathbf{D}_t^{-1}. \tag{14}$$

Using the above update equation, the overall complexity is $O(N^2M + M^3)$, which grows quadratically with N.

Finally, a binary occupancy map $\hat{\mathbf{g}} \in \{0,1\}^N$ is obtained by thresholding the estimated probabilities in $\hat{\mathbf{f}}$ with η_{th}.

TABLE I

ANGULAR SCAN NMSE FOR NUSCENES SCENE-165

Methods	NMSE for LiDAR	NMSE for Radar
[5]	0.41	0.37
[13]	0.37	0.38
Proposed	0.37	0.17

TABLE II

IOBB FOR NUSCENES SCENE-165

Object ID	Object Type	IoBB for LiDAR			IoBB for Radar		
		[5]	**[13]**	**Prop.**	**[5]**	**[13]**	**Prop.**
1	Car	0.14	0	0.10	0.10	0.31	0.069
2	Car	0.38	0.59	0.18	0	0	0.059
3	Car	0.28	0.17	0.056	0.028	0	0.083
4	Car	0	0	0	0	0	0.063
5	Car	0.18	0.15	0.091	0	0	0.061
6	Car	0.33	0.15	0.15	0.030	0	0.15
7	Pedestrian	0	0.5	0.5	0	0	1

TABLE III

IOBB FOR NUSCENES SCENE-204

Object ID	Object Type	IoBB for LiDAR			IoBB for Radar		
		[5]	**[13]**	**Prop.**	**[5]**	**[13]**	**Prop.**
1	Pedestrian	0	0	1	0	0	0
2	Pedestrian	0	0.5	1	0	0	0
3	Pedestrian	0	1	0.50	0	0	0
4	Car	0.60	0.40	0.27	0	0.012	0.16
5	Van	0.74	0.51	0.28	0	0	0.016
6	Car	0	0.50	1	0	0	0
7	Pedestrian	0.5	0	0	0	0	0
8	Pedestrian	1	0.50	0.5	0	0	0
9	Car	0.48	0.52	0.26	0.083	0.25	0.21
10	Pedestrian	0.25	0.25	0.75	0	0	0
11	Car	0.69	0.39	0.31	0.028	0.028	0.17

TABLE IV

ANGULAR SCAN NMSE FOR NUSCENES SCENE-204

Methods	NMSE for LiDAR	NMSE for Radar
[5]	0.41	0.65
[13]	0.50	0.56
Proposed	0.37	0.46

Specifically, for any $1 \leq n \leq N$, we obtain

$$\hat{g}[n] = \begin{cases} 0, & \hat{f}[n] < \eta_{\text{th}} \\ 1, & \hat{f}[n] \geq \eta_{\text{th}}. \end{cases} \tag{15}$$

The estimated binary occupancy map provides information about potential obstacles (indicated by 1) and free cells (indicated by 0) surrounding the ego vehicle.

IV. PERFORMANCE EVALUATION

In this section, we compare the occupancy grid maps constructed using our approach with two other algorithms [5], [13]. We use 2-D grids of equal size, each measuring 0.5 × 0.5 m. The size of the generated maps is 40 × 40 m leading to $N = 6400$ grid cells in total. Our results were obtained by hand-tuning the parameters of the corresponding algorithms. Specifically, the free-space line segments are sampled with a resolution of 1 m for [13] and 0.5 m for the proposed approach. The labels y_{occ} and y_{free} are set to 1 and 0, respectively. We set the kernel size as 1 m for [13] to exploit the spatial correlation between neighboring cells. The coupling parameter

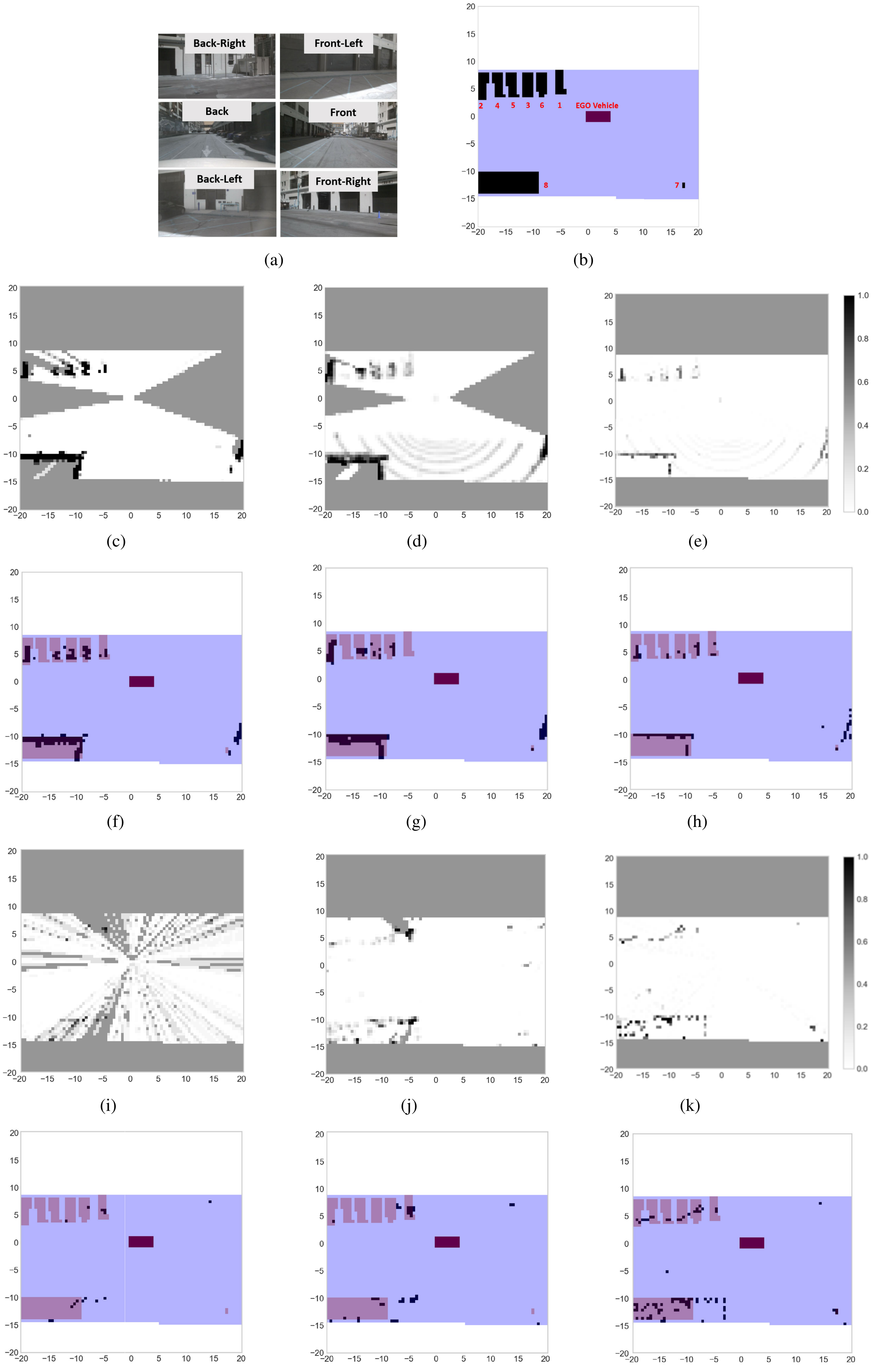

(a) (b)

(c) (d) (e)

(f) (g) (h)

(i) (j) (k)

(l) (m) (n)

Fig. 2. LiDAR and radar occupancy grid mapping results for scene-165 from the nuScenes dataset. (a) Camera images. (b) Ground truth map. (c) Occupancy values [5]. (d) Occupancy values [13]. (e) Occupancy values (proposed). (f) Occupancy map [5]. (g) Occupancy map [13]. (h) Occupancy map (proposed). (i) Occupancy values [5]. (j) Occupancy values [13]. (k) Occupancy values (proposed). (l) Occupancy map [5]. (m) Occupancy map [13]. (n) Occupancy map (proposed).

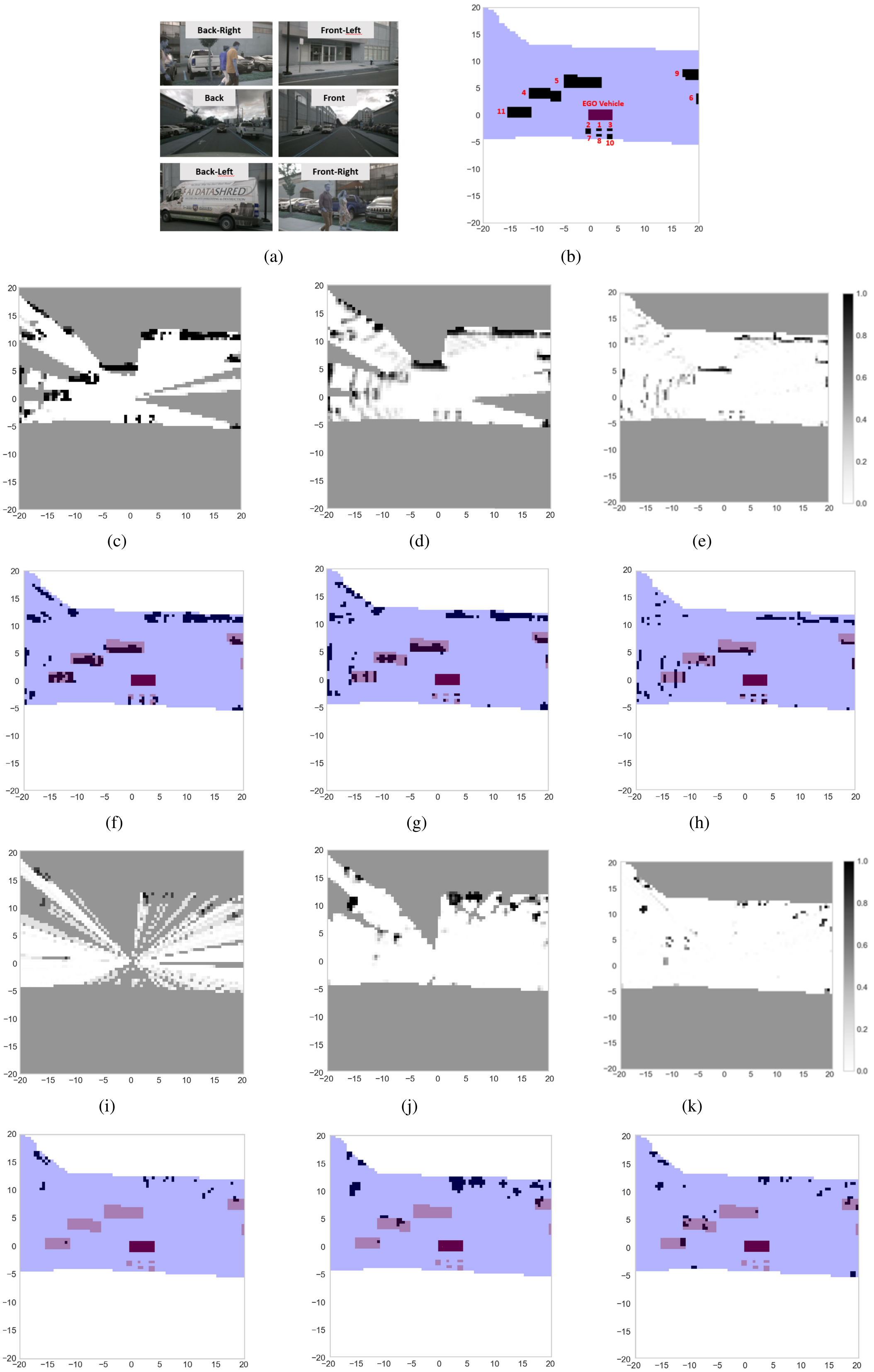

(a) (b)

(c) (d) (e)

(f) (g) (h)

(i) (j) (k)

(l) (m) (n)

Fig. 3. LiDAR and radar occupancy grid mapping results for scene-204 from the nuScenes dataset. (a) Camera images. (b) Ground truth map. (c) Occupancy values [5]. (d) Occupancy values [13]. (e) Occupancy values (proposed). (f) Occupancy map [5]. (g) Occupancy map [13]. (h) Occupancy map (proposed). (i) Occupancy values [5]. (j) Occupancy values [13]. (k) Occupancy values (proposed). (l) Occupancy map [5]. (m) Occupancy map [13]. (n) Occupancy map (proposed).

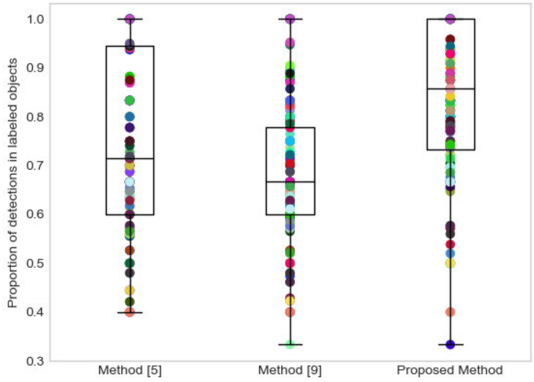

Fig. 4. Distribution of the proportion of detected objects to labeled objects in the ground truth map. The analysis is carried out on 200 samples from the nuScenes dataset.

β of our PC-SBL-based algorithm is set to 1, prior distribution parameter a is set to 0.5, and b, c, and d are set to 0 as suggested in [15]. When a radar point cloud is used for the proposed approach, we set $\Omega = 2^\circ$ and Δ to 2 grid cells for the conical beam. Finally, to generate the binary occupancy maps, the threshold η_{th} is chosen as 0.5 for the benchmark algorithms and 0.3 for the proposed approach.

A. Performance Metrics

To evaluate the accuracy of the map, we employ two metrics: angular scan NMSE, where the scan is done at the ego vehicle, and IoBB. For the ground truth map, we define $\mathbf{d}$ as a vector that comprises the distances from the ego vehicle to the first occupied cell along each direction of the angular scan. In particular, $d[i]$ represents the maximum distance the ego vehicle can travel in direction i before encountering an obstacle. A similar vector $\hat{\mathbf{d}}$ is defined for the estimated occupancy map. The angular scan NMSE is defined as $\text{NMSE} = (\|\mathbf{d} - \hat{\mathbf{d}}\|^2/\|\mathbf{d}\|^2)$. We extend the metric in [23] to define IoBB as the ratio of the overlapping area between the occupied cells and the ground truth boundary boxes to the area of the ground truth boundary boxes. Note that IoBB lies between 0 and 1, and a score larger than 0 indicates the detection of the corresponding obstacle.

B. Results Based on LiDAR and Radar Point Clouds From the nuScenes Dataset

We first consider occupancy map estimation with LiDAR and radar point clouds from the nuScenes dataset. The nuScenes dataset contains scenes from the cities of Boston and Singapore. It includes image views from six cameras (front center, front left, front right, rear center, rear left, and rear right), one LiDAR, and five radars (one front, front left corner, front right corner, rear left corner, and rear right corner) with bird's eye view (BEV) object annotations [16]. We chose this dataset as our main evaluation source because it is one of the first large-scale autonomous driving sensor datasets widely used to evaluate automotive perception. It also provides street map information and BEV bounding box labels for many object classes on the street. The radar data, however, are much sparser than the LiDAR data, and the low detection performance of the radar [24] in the nuScenes campaign is a known issue.

The assessment is done both qualitatively and using the NMSE and IoBB metrics that measure the difference from the ground truth. The ground truth map is created from nuScenes using the locations and sizes of the boundary boxes within the focus drivable region. The 2-D footprints of the boundary boxes of the dynamic objects inside the focus area were drawn and used as the ground truth representation of the targets.

We first consider scene-165, in which the focus area contains seven objects with labels: six cars at the rear and one pedestrian on the front right of the ego vehicle. There is also a fence in the rear right corner, which is manually labeled as object 8. The ground truth and estimated occupancy maps for scene-165 are shown in Fig. 2. The better performance of our algorithm in detecting objects can be observed from the computed NMSE metric in Table I and the IoBB values in Table II. For LiDAR, the NMSE values are comparable, while the pedestrian is detected by our proposed method. For radar, cars 2, 4, and 5 and pedestrian are not detected in methods such as [5] and [13], while our method does.

We now consider scene-204, in which the focus area contains 11 labeled objects, including four cars and six pedestrians to the right of the ego vehicle. As two of the pedestrians are close to each other, they are represented with a single boundary box, leading to five boundary boxes for pedestrians in Fig. 3(b). Fig. 3 shows that [13] and our approach successfully detect all the cars, whereas [5] does not detect the car at the right end of the road. Furthermore, the three methods demonstrate varying performances in detecting pedestrians with IDs 1, 2, 3, 7, and 8, positioned to the right of the car. The IoBB values in Table III indicate that [5] detects two of the pedestrians, [13] detects four of them, and our approach detects five of them. The pedestrian with ID 1 remains undetected by all algorithms since this pedestrian's visibility is obstructed by a neighboring pedestrian. The better performance of our algorithm in pedestrian detection is also reflected in the lower NMSE value in Table IV. The results with radar are inferior for all three methods, with all the pedestrians undetected. Our method performs nominally better than [5] and [13] in detecting the larger objects, e.g., the van is detected by our method, while the reference methods missed it.

We finally analyze the statistical performance of the proposed method with [5] and [13] using the LiDAR point clouds corresponding to 200 samples. As a metric, we consider the ratio of detected objects in the estimated occupancy map to the number of actual labeled objects in the ground truth. From Fig. 4, we infer that the median of this metric for our method (0.84) is higher than those of the other methods (0.74 for [5] and 0.69 for [13]); the variance of our method is 0.02, while [5] has a higher value of 0.03 and a similar value of 0.02 for [13].

C. Results Based on LiDAR and Radar Point Cloud From RADIal Dataset

The RADIal dataset contains a single front-looking camera, LIDAR, and radar, with object bounding boxes indicated

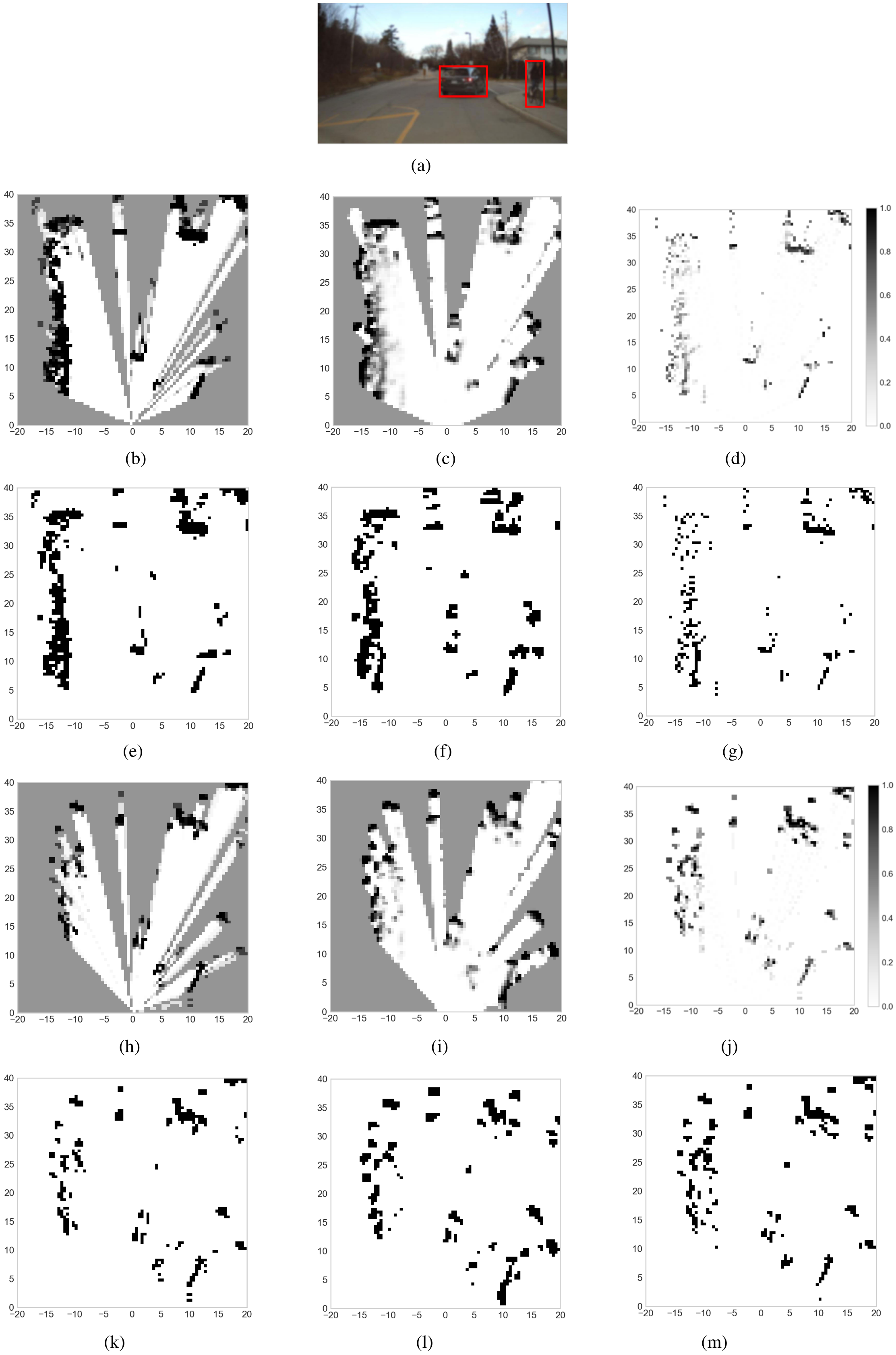

Fig. 5. LiDAR and radar occupancy grid mapping results for scene-2681 from RADIal dataset. (a) Camera images. (b) Occupancy values [5]. (c) Occupancy values [13]. (d) Occupancy values (proposed). (e) Occupancy map [5]. (f) Occupancy map [13]. (g) Occupancy map (proposed). (h) Occupancy values [5]. (i) Occupancy values [13]. (j) Occupancy values (proposed). (k) Occupancy map [5]. (l) Occupancy map [13]. (m) Occupancy map (proposed).

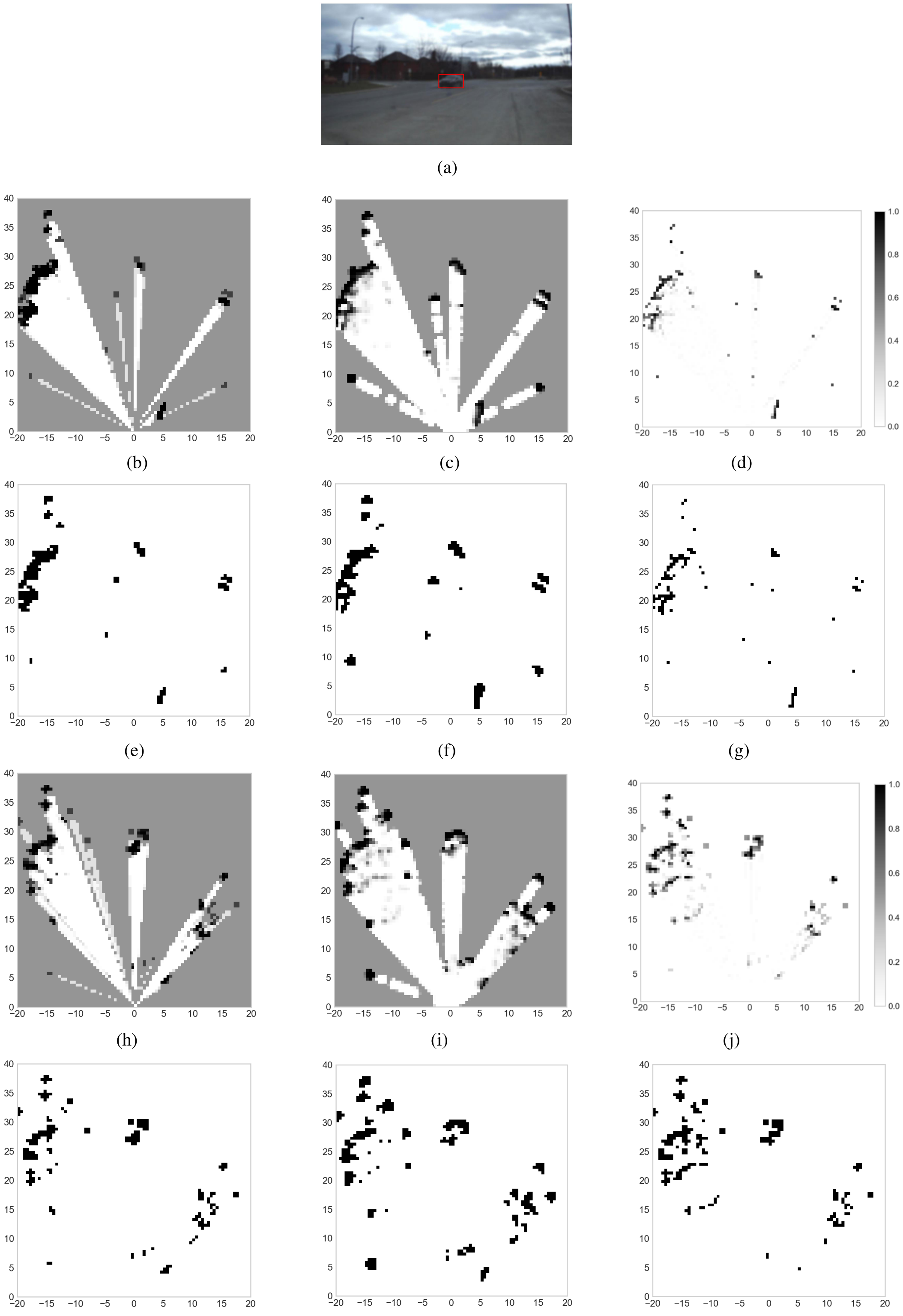

(a)

(b) (c) (d)

(e) (f) (g)

(h) (i) (j)

(k) (l) (m)

Fig. 6. LiDAR and radar occupancy grid mapping results for scene-3218 from RADIal dataset. (a) Camera images. (b) Occupancy values [5]. (c) Occupancy values [13]. (d) Occupancy values (proposed). (e) Occupancy map [5]. (f) Occupancy map [13]. (g) Occupancy map (proposed). (h) Occupancy values [5]. (i) Occupancy values [13]. (j) Occupancy values (proposed). (k) Occupancy map [5]. (l) Occupancy map [13]. (m) Occupancy map (proposed).

by 2-Di camera coordinates [17], [18]. This dataset is our secondary performance evaluation source since its radar point cloud density is much higher than that in nuScenes, although it has no street annotations or BEV bounding boxes. Hence, we shall limit our evaluation to a qualitative comparison.

In Fig. 5, there is a car (labeled in the dataset) and a cyclist (manually labeled) in the scene as seen in the camera view. From the LiDAR results in Fig. 6(b)–(g), it is observed that the discrimination between the cyclist and the adjacent street pole is better in [13] and our method compared to [5]. All the methods based on LiDAR and radar data perform well in detecting both the car and estimating the occupancy map.

In Fig. 6, there is one car in the camera view. All the methods perform well in car detection and map estimation, while the radar results provide a better representation of the car in comparison to the LiDAR results in Fig. 6(b)–(g). This can be attributed to the better detection capabilities of radar in comparison to LiDAR for objects at longer ranges.

V. CONCLUSION AND DISCUSSION

Occupancy map estimation based on PC-SBL was considered using point clouds that originate from automotive LiDAR or radar sensor measurements. When applying the proposed approach to LiDAR point cloud data, better performance is evident in two aspects than the benchmarks. First, the occupancy values due to road reflections are suppressed due to the use of a sparse prior on the occupancy map and due to exploiting spatial correlation. Second, the proposed method is able to detect smaller obstacles like pedestrians better. Finally, we observe that our method results in low IoBB values for the detected objects than the other methods. This is because our method promotes a sparse prior on the occupancy map. This trend is also observed in the evaluation of the proposed method with radar point cloud data. Occupancy map estimation with LiDAR data is better than with radar data on the nuScenes dataset, which can be attributed to LiDAR point cloud data being one to two orders denser compared to radar point cloud data [16]. On the RADIal dataset, the occupancy map estimates were comparable with both LiDAR and radar point clouds, with radar providing better detection of objects at longer ranges.

It is known that under adverse weather scenarios, a radar point cloud provides better occupancy grid estimates, while in some scenarios, the high-resolution capabilities of a LiDAR or semantic understanding capabilities of a camera can be advantageous. In future work, early/middle fusion of sensor point clouds from multiple modalities, such as camera, LiDAR, and radar using Bayesian learning approaches to improve occupancy map estimation, will be explored. We also intend to explore the mapping techniques based on other machine learning techniques, such as deep learning. Furthermore, path-planning solutions for automated driving based on the occupancy maps are also an interesting avenue for future work that builds upon past works [8], [9].

REFERENCES

[1] E. Marti, M. A. de Miguel, F. Garcia, and J. Perez, "A review of sensor technologies for perception in automated driving," *IEEE Intell. Transp. Syst. Mag.*, vol. 11, no. 4, pp. 94–108, Sep. 2019.

[2] A. Pandharipande et al., "Sensing and machine learning for automotive perception: A review," *IEEE Sensors J.*, vol. 23, no. 11, pp. 11097–11115, Jun. 2023.

[3] A. Elfes, "Using occupancy grids for mobile robot perception and navigation," *Computer*, vol. 22, no. 6, pp. 46–57, Jun. 1989.

[4] D. Nuss, M. Stuebler, and K. Dietmayer, "Consistent environmental modeling by use of occupancy grid maps, digital road maps, and multi-object tracking," in *Proc. IEEE Intell. Vehicles Symp.*, Jun. 2014, pp. 1371–1377.

[5] S. Thrun, W. Burgard, and D. Fox, *Probabilistic Robotics* (Intelligent Robotics and Autonomous Agents series). Cambridge, MA, USA: MIT Press, 2005.

[6] A. Birk and S. Carpin, "Merging occupancy grid maps from multiple robots," *Proc. IEEE*, vol. 94, no. 7, pp. 1384–1397, Jul. 2006.

[7] M. Schreiber, V. Belagiannis, C. Gläser, and K. Dietmayer, "A multi-task recurrent neural network for end-to-end dynamic occupancy grid mapping," in *Proc. IEEE Intell. Vehicles Symp. (IV)*, Jun. 2022, pp. 315–322.

[8] S. Mentasti and M. Matteucci, "Multi-layer occupancy grid mapping for autonomous vehicles navigation," in *Proc. AEIT Int. Conf. Electr. Electron. Technol. Automot. (AEIT AUTOMOTIVE)*, Jul. 2019, pp. 1–6.

[9] C. Diehl, E. Feicho, A. Schwambach, T. Dammeier, E. Mares, and T. Bertram, "Radar-based dynamic occupancy grid mapping and object detection," in *Proc. IEEE 23rd Int. Conf. Intell. Transp. Syst. (ITSC)*, Sep. 2020, pp. 1–6.

[10] F. Xu, H. Wang, B. Hu, and M. Ren, "Road boundaries detection based on modified occupancy grid map using millimeter-wave radar," *Mobile Netw. Appl.*, vol. 25, no. 4, pp. 1496–1503, Aug. 2020.

[11] E. Kaufman, T. Lee, Z. Ai, and I. S. Moskowitz, "Bayesian occupancy grid mapping via an exact inverse sensor model," in *Proc. Amer. Control Conf. (ACC)*, Jul. 2016, pp. 5709–5715.

[12] S. T. O'Callaghan and F. T. Ramos, "Gaussian process occupancy maps," *Int. J. Robot. Res.*, vol. 31, no. 1, pp. 42–62, Jan. 2012.

[13] K. Doherty, J. Wang, and B. Englot, "Bayesian generalized kernel inference for occupancy map prediction," in *Proc. IEEE Int. Conf. Robot. Autom. (ICRA)*, May 2017, pp. 3118–3124.

[14] M. Kurdej, J. Moras, V. Cherfaoui, and P. Bonnifait, "Map-aided evidential grids for driving scene understanding," *IEEE Intell. Transp. Syst. Mag.*, vol. 7, no. 1, pp. 30–41, Jan. 2015.

[15] J. Fang, Y. Shen, H. Li, and P. Wang, "Pattern-coupled sparse Bayesian learning for recovery of block-sparse signals," *IEEE Trans. Signal Process.*, vol. 63, no. 2, pp. 360–372, Jan. 2015.

[16] H. Caesar et al., "nuScenes: A multimodal dataset for autonomous driving," in *Proc. IEEE/CVF Conf. Comput. Vis. Pattern Recognit. (CVPR)*, Jun. 2020, pp. 11621–11631.

[17] RADIal dataset. (2021). [Online]. Available: https://github.com/valeoai/RADIal

[18] J. Rebut, A. Ouaknine, W. Malik, and P. Pérez, "Raw high-definition radar for multi-task learning," in *Proc. IEEE/CVF Conf. Comput. Vis. Pattern Recognit. (CVPR)*, Jun. 2022, pp. 17021–17030.

[19] Ç. Önen, A. Pandharipande, G. Joseph, and N. J. Myers, "LiDAR-based occupancy grid map estimation exploiting spatial sparsity," in *Proc. IEEE SENSORS*, Nov. 2023, pp. 1–4.

[20] W. J. Fleming, "New automotive sensors—A review," *IEEE Sensors J.*, vol. 8, no. 11, pp. 1900–1921, Nov. 2008.

[21] K. Irie and M. Tomono, "Localization and road boundary recognition in urban environments using digital street maps," in *Proc. IEEE Int. Conf. Robot. Autom.*, May 2012, pp. 4493–4499.

[22] M. E. Tipping, "Sparse Bayesian learning and the relevance vector machine," *J. Mach. Learn. Res.*, vol. 1, pp. 211–244, Jun. 2001.

[23] V. Jiménez, J. Godoy, A. Artuñedo, and J. Villagra, "Object-wise comparison of LiDAR occupancy grid scan rendering methods," *Robot. Auto. Syst.*, vol. 161, Mar. 2023, Art. no. 104363.

[24] S. Muckenhuber, E. Museljic, and G. Stettinger, "Performance evaluation of a state-of-the-art automotive radar and corresponding modeling approaches based on a large labeled dataset," *J. Intell. Transp. Syst.*, vol. 26, no. 6, pp. 655–674, Nov. 2022.

Çağan önen received the B.Sc. degree in electrical and electronics engineering from Bilkent University, Ankara, Turkey, in 2021, and the M.Sc. degree in electrical engineering from the Delft University of Technology, Delft, The Netherlands, in 2023.

His research interests include wireless communications and signal processing.

Ashish Pandharipande (Senior Member, IEEE) received the M.S. degree in electrical and computer engineering, the M.S. degree in mathematics, and the Ph.D. degree in electrical and computer engineering from the University of Iowa, Iowa City, IA, USA, in 2000, 2001, and 2002, respectively.

Subsequently, he was a Postdoctoral Researcher at the University of Florida, Gainesville, FL, USA; a Senior Researcher at the Samsung Advanced Institute of Technology, Suwon, South Korea; a Senior Scientist at Philips Research, Eindhoven, The Netherlands; and the Lead Research and Development Engineer at Signify, Eindhoven. He has held visiting positions at AT&T Laboratories, Murray Hill, NJ, USA, and the Department of Electrical Communication Engineering, Indian Institute of Science, Bengaluru, India. He is currently Innovation Director of NXP Semiconductors, Eindhoven. His research interests are in sensing, networking and controls, data analytics, and their applications in domains such as autonomous mobility, smart lighting systems, energy monitoring and control, and cognitive wireless systems. He has around 200 international conference and journal publications and more than 100 patent grants/applications in these fields.

Dr. Pandharipande is a Senior Editor of IEEE SIGNAL PROCESSING LETTERS, a Topical Area Editor of IEEE SENSORS JOURNAL, and an Associate Editor of IEEE JOURNAL OF BIOMEDICAL AND HEALTH INFORMATICS.

Geethu Joseph (Member, IEEE) received the B.Tech. degree in electronics and communication engineering from the National Institute of Technology Calicut, Kozhikode, India, in 2011, and the M.E. degree in signal processing and the Ph.D. degree in electrical communication engineering (ECE) from the Indian Institute of Science (IISc), Bengaluru, India, in 2014 and 2019, respectively.

She was a Postdoctoral Fellow with the Department of Electrical Engineering and Computer Science, Syracuse University, Syracuse, NY, USA, from 2019 to 2021. She is currently a tenured Assistant Professor with the Signal Processing Systems Group, Delft University of Technology, Delft, The Netherlands. Her research interests include statistical signal processing, network control, and machine learning.

Dr. Joseph was awarded the 2022 IEEE SPS Best Ph.D. Dissertation Award and the 2020 SPCOM Best Doctoral Dissertation Award. She was a recipient of the Prof. I. S. N. Murthy Medal in 2014 for being the Best M.E. (signal processing) Student at the Department of Electrical Communication Engineering, IISc, and the Seshagiri Kaikini Medal for the Best Ph.D. Thesis of the Department of Electrical Communication Engineering, IISc, for the year 2019–2020. She is an Associate Editor of the IEEE SENSORS JOURNAL and an active reviewer for major journals and conferences in signal processing, communications, and control theories.

Nitin Jonathan Myers (Member, IEEE) received the B.Tech. and M.Tech. degrees in electrical engineering from the Indian Institute of Technology (IIT) Madras, Chennai, India, in 2016, and the Ph.D. degree in electrical and computer engineering (ECE) from The University of Texas at Austin (UT Austin), Austin, TX, USA, in 2020.

He is currently an Assistant Professor with the Delft Center for Systems and Control, Delft University of Technology (TU Delft), Delft, The Netherlands. Prior to joining TU Delft, he was a Senior Engineer with the 5G Modem Research and Development Team, Samsung Semiconductor Inc., San Diego, CA, USA. His research interests include optimization and multidimensional signal processing, with applications to communications and sensing.

Dr. Myers received the DAAD WISE Scholarship in 2014 and a Silver Medal and the Institute Merit Prize in 2016 during his undergraduate days at IIT Madras. At UT Austin, he received the University Graduate Continuing Fellowship for the term 2019–2020, the 2018 and 2019 ECE Research Awards, and the 2018 ECE Professional Development Award from the Cockrell School of Engineering. He was recognized as an exemplary reviewer by IEEE TRANSACTIONS ON COMMUNICATIONS in 2019 and the IEEE WIRELESS COMMUNICATIONS LETTERS in 2018. His research won the IEEE ICASSP 2020 Video Contest runner-up and the Best Student Paper Award at IEEE SPAWC 2022. Recently, he was recognized by TU Delft as the Best Lecturer in the second year of the bachelor's program in mechanical engineering for the term of 2021–2022.